RSC Advances

ROYAL SOCIETY OF CHEMISTRY

PAPER

View Article Online
View Journal | View Issue

Cite this: *RSC Adv.*, 2025, **15**, 25625

Symmetry-breaking-engineered in-plane bulk photovoltaic effect in van der Waals WS_2/CrOCl heterostructure†

Hong Zhou,‡[a] Yuehua Wei,‡[bc] Wei Luo,‡[c] Congbing Tan, *[a] Zhiyuan Dou,[a] Zhongqiang Hu,[a] Qianyi Li[a] and Xiaoming Zheng *[a]

The bulk photovoltaic effect (BPVE), arising from symmetry breaking, has potential to attain conversion efficiencies which surpass Shockley–Queisser limit. Here, we achieve in-plane BPVE in WS_2/CrOCl heterostructure, attributed to broken-symmetry interfaces by stacking the WS_2 onto anisotropic CrOCl. The breaking symmetry is evidenced by the asymmetric second harmonic generation and angle dependent Raman spectra. The linear *I*–*V* curves demonstrate formation of the BPVE with an open-circuit voltage of 34 mV. Meanwhile, the photocurrent response across the entire channel under zero bias exhibits obvious polarized angle dependence with photocurrent anisotropy ratio of 3.29. The separation of the photogenerated carriers is caused by electric field, originating from in-plane polarization, as demonstrated by piezoresponse force microscopy. This study enhances the understanding of the BPVE and suggests novel strategies for future self-powered devices.

Received 18th May 2025
Accepted 3rd July 2025

DOI: 10.1039/d5ra03506f

rsc.li/rsc-advances

1 Introduction

Photovoltaic energy is considered one of the most promising renewable energy sources. Photocurrent generation in traditional photovoltaics depends on p–n junctions with the photoelectric efficiency constrained by the Shockley–Queisser (SQ) limit.[1,2] Fortunately, the bulk photovoltaic effect (BPVE), a second-order nonlinear optical effect occurring in non-centrosymmetric materials, provides a potential solution to overcome the SQ limit,[1,3] enhancing conversion efficiency. BPVE refers to a phenomenon where a steady-state photocurrent is generated in non-centrosymmetric materials under illumination and zero bias.[4,5] In contrast to traditional photovoltaics that achieve charge separation *via* the built-in electric field formed by a p–n junction, the charge separation in BPVE arises from the spontaneous polarization caused by the non-centrosymmetric structure.[6] Over the past years, BPVE has been observed in the conventional ferroelectric materials, such as $BiFeO_3$,[7,8] $BaTiO_3$.[9,10] However, depolarization fields increase with decreasing thickness of these ferroelectric materials and spontaneous polarization is reduced or becomes unstable.[11] Moreover, wide bandgap in these ferroelectric materials leads to lower carrier mobility and short absorbable wavelength range.[12–14]

Given the challenge of BPVE in conventional ferroelectric materials, two-dimensional (2D) ferroelectric materials with narrow bandgap exhibit stable polarization in the nanoscales and tunable bandgaps by thickness.[15–17] For example, the polarization intensity of a single layer α-In_2Se_3 (0.7 nm) can reach up to 80 pC m^{-1}.[18,19] In addition, α-In_2Se_3 exhibits exceptional terahertz radiation efficiency driven by BPVE in the infrared region, achieving an efficiency approximately eight times that of standard ZnTe.[20–22] However, spontaneous polarization in 2D materials is usually not high enough compared to conventional materials.[23,24] It is necessary to explore new strategies to enhance the polarization intensity. In recent years, researchers have employed various methods to disrupt the symmetry of 2D materials, thereby effectively enhancing polarization.[25–28] For instance, a Janus MoSSe monolayer with an asymmetric atomic lattice can be synthesized by substituting the top sulfur (S) atoms with selenium (Se) atoms in the MoS_2, enhancing out-of-plane polarization.[25] Moreover, through interlayer sliding, bilayer MoS_2 or bilayer WTe_2 materials can enhance the polarization effect, thereby improving the optoelectronic response.[29] These methods demand advanced craftsmanship and are difficult to popularize.

An effective approach for inducing polarization at the material interfaces is to stack 2D materials with different rotational symmetries, such as C_2 and C_3.[30–34] Among these, materials with C_2 symmetry play a crucial role in enhancing

[a]*Hunan Provincial Key Laboratory of Intelligent Sensors and Advanced Sensor Materials, School of Physics and Electronic Science, Hunan University of Science and Technology, Xiangtan, 411201, China. E-mail: 1080098@hnust.edu.cn; cbtan@xtu.edu.cn*

[b]*School of Physics and Optoelectronics, Xiangtan University, Xiangtan 411105, China*

[c]*College of Science, National University of Defense Technology, Changsha, 410073, China*

† Electronic supplementary information (ESI) available. See DOI: https://doi.org/10.1039/d5ra03506f

‡ These authors contributed equally to the work.

polarization effects of the interface because they show specific rotational symmetry properties. For instance, polarization was successfully achieved at the asymmetric interface by combining monolayer WSe_2 and black phosphorus (BP) crystals. As a result, a spontaneous photocurrent was observed along the direction of in-plane polarization.[30] BPVE has been realized in the MoS_2/BP heterostructure.[35] However, the realization of BPVE by symmetry engineering is still rare, only TMD/BP heterostructure systems have were reported to induce BPVE. In addition, anisotropic BP exhibits poor stability in air.[35] Thus, it is important to explore a new low symmetry and stable material.

Low-symmetry CrOCl is an air-stable van der Waals (vdW) insulator,[36–39] serving as an ideal candidate for inducing polarization in future heterostructures. Herein, we propose an effective strategy to induce BPVE by breaking WS_2/CrOCl interfacial symmetry. The symmetry-breaking at the heterointerface is verified by employing second harmonic generation (SHG) and angle dependent Raman spectra. The non-zero intercept in the linear *I–V* curve demonstrates the presence of the BPVE under laser irradiation, which can be attributed to the symmetry interfacial breaking. The photocurrent distribution across the entire channel shows polarized angle dependence by photocurrent mapping under linearly polarized laser light and zero bias. It was observed that the WS_2/CrOCl heterostructure exhibits in-plane polarization using piezoelectric force microscopy (PFM) which is identified as a key factor contributing to BPVE. Our research provides new material system for the development of BPVE and provide insights for the development of next-generation self-powered ultrathin photodetectors.

2 Experimental

Few-layer WS_2 (Shanghai Onway Technology Co., Ltd, Shanghai, China) were mechanically exfoliated from the corresponding respective single crystals by a scotch tape method. WS_2/CrOCl heterostructure was constructed employing the dry transfer method. In the preparation process, a polyvinyl butyral (PVB) film is utilized for bonding and transferring two-dimensional materials due to its excellent transparency and resolvability in anhydrous ethanol. To enhance handling and facilitate removal, the thickness of the PVB films in the study is approximately 150 μm. However, a polydimethylsiloxane (PDMS) film serves as the intermediate transition layer and the heat-releasing layer owing to its high transparency and distinct viscosities on its two surfaces. To facilitate the heat release and transparency, the release temperature and thickness of the PDMS film are 60 °C and 1 mm, respectively. The WS_2 flake was aligned with the CrOCl flake and transferred onto it with the aid of a display that shows the microscope view of the sample on the transfer stage. Specifically, WS_2 was lifted using PVB and its shape was outlined on the display. Then, by locating the target CrOCl flake and rotating the Si/SiO_2 substrate on which it was placed, the WS_2 and CrOCl flakes were precisely aligned. Finally, anhydrous ethanol was utilized to remove the PVB. The Ti/Au conducting electrodes were fabricated on the surface of WS_2/CrOCl heterostructure using standard electron beam lithography (Raith e-LINE Plus, Germany) and e-beam evaporation (Kurt J. Lesker PVD75, USA). SHG measurements were conducted using the MStarter SHG microscope spectrometer, with pulses shorter than 2 ps at 1020 nm wavelength and a repetition rate of 40 MHz. The laser was focused on a spot with a diameter of 1 μm with a 100× objective. The crystal orientations of the WS_2 and WS_2/CrOCl samples are determined from their polarized-SHG measurements. Raman spectra and Raman intensity ratios were recorded to ascertain the crystal directions of CrOCl using alpha 300 R Raman spectrophotometer (WITec, Germany) with a laser wavelength of 532 nm. The WS_2/CrOCl device was positioned on the electrical measurement platform for the Raman-photocurrent spectroscopy setup. The polarization angle was adjustable by using a half-wave plate, and a focused laser beam with a wavelength of 532 nm was directed onto the sample through a 100× microscope objective. By changing the angle between the polarizer and the half-wave plate, the photocurrent signals generated by the polarization could be detected with a Keithley 2636B Dual-channel System Source Meter. The heterostructure was examined by a commercial scanning probe microscope (Asylum Research, MFP-3D infinity) in tapping mode to observe the morphology and in the dual AC resonance tracking (DART) piezoresponse mode (both in-plane and out-of-plane modes) to analyze the polarization characteristics.

3 Results and discussion

3.1 Design of symmetry-broken WS_2/CrOCl heterostructure

WS_2 is stacked onto CrOCl to create a symmetry-mismatch heterostructure because the two materials exhibit distinct rotational and mirror symmetries. CrOCl, classified under the orthorhombic system, displaces twofold-rotational symmetry (C_2) and a set of mirror planes, while WS_2 has threefold-rotational symmetry (C_3) and mirror planes along the armchair direction (Fig. 1a and b). Because the threefold and twofold rotational symmetries are mismatched, the WS_2/CrOCl heterostructure interface lacks rotational symmetry. Interestingly, mirror symmetry can still be maintained if the mirror planes of both WS_2 and CrOCl are aligned parallel (Fig. 1c). Furthermore, a stripe moiré pattern can be observed in the interface (Fig. 1c), which is analogous to those observed in WSe_2/BP and MoS_2/CrOCl,[30,34] which differs from the hexagonal moiré patterns in twisted graphene.[40] Due to the mismatch in lattice periodicity and symmetry between WS_2 and CrOCl, leading to the formation of stripe moiré patterns.[41–44] Current experimental studies have observed the formation of moiré patterns in the graphene/ReS_2 heterostructure and graphene/BP structure.[42,43,45] The pattern reveals the trigonal symmetry of WS_2 and the anisotropic moiré potential of CrOCl, which together give rise to the in-plane polarity induced at the interface.[30,33]

To understand the properties of the WS_2/CrOCl interface, WS_2 was transfer onto CrOCl on a silicon wafer with a 300-nm-thick SiO_2 layer using the dry transfer method (Fig. 1d). Prior to stacking, the crystal directions were determined by the second harmonic generation (SHG) in WS_2 (Fig. 1e) and the Raman intensity ratio in CrOCl (Fig. S1†). In order to characterize the

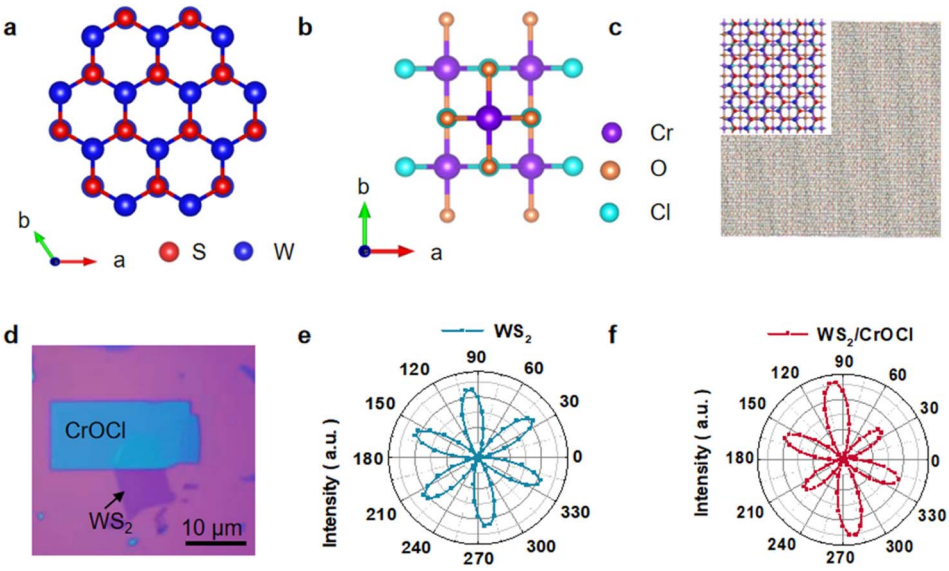

Fig. 1 Typical features of WS_2/CrOCl heterostructure. (a) Schematic illustrations of crystal lattice structure for WS_2. (b) Schematic illustrations of crystal lattice structure for CrOCl. Red, blue, purple, orange and light blue spheres represent S, W, Cr, O and Cl atoms, respectively. (c) Moiré patterns of the WS_2/CrOCl heterointerface. The inset shows the corresponding lattice structure. (d) Optical microscope image of WS_2/CrOCl on Si/SiO_2 substrate. WS_2 flake on top of CrOCl flake. (e) Polar plot of angle-resolved second harmonic generation (SHG) pattern of WS_2. (f) Polar plot of angle-resolved second harmonic generation (SHG) pattern of WS_2/CrOCl. Dots present the experiment data.

structural asymmetry at the WS_2/CrOCl interface, the angle-resolved SHG were performed on both WS_2 and the heterostructure. In pristine WS_2, SHG signal shows a sixfold-symmetry pattern with maxima of SHG intensity along its armchair direction (Fig. 1e), suggesting the D_{3h} point group.[46,47] While the SHG signal of WS_2/CrOCl heterostructure displays an additional twofold component superimposed on the six symmetric petals (Fig. 1f). Such a twofold component does not originate from the C_3-symmetric lattice of WS_2 itself. As shown in Fig. S2,† the intensity is weaker and the polar plots do not exhibit obvious symmetry in pristine CrOCl, confirming that CrOCl itself does not contribute to the SHG signal of the heterostructure.[34] These phenomena imply that the SHG signal in heterostructure mainly originates from WS_2 rather than CrOCl. Additionally, the angle-dependent Raman spectra exhibit typical twofold symmetry in the heterostructure (Fig. S3†). Therefore, the asymmetric SHG pattern (Fig. 1f) and the angle-dependent Raman spectra (Fig. S3†) suggest symmetry breaking at the heterostructure interface which indicates potential for BPVE generation in this system.[30,35]

3.2 Bulk photovoltaic effect in the WS_2/CrOCl devices

To examine the impact of the broken inversion symmetry, photoresponse of a WS_2/CrOCl heterostructure was measured. Here, the device was fabricated by transferring few-layer WS_2 onto CrOCl, and then the Ti (5 nm)/Au (80 nm) electrodes were prepared using a conventional semiconductor process (Fig. 2a). As illustrated in Fig. 2b, the electrodes were deposited on the WS_2/CrOCl flake without formation of p–n junction. Notably, both electrodes were fabricated using the same Ti/Au material and symmetrically contacted the heterostructure region. This symmetric configuration eliminates differences in Seebeck coefficients at the contacts, thereby the spontaneous current does not primarily originate from the photothermoelectric effect.[48,49] On account of the insulation properties of CrOCl, the transport of the photogenerated carriers hardly occurs in CrOCl. In contrast to TMD/BP heterostructure systems, the photocurrent is not only contributed by the photogenerated carriers at the heterointerface but also linked to the charge carriers transferred from the bottom BP.[30,35] Consequently, we can directly observe the electrical characteristics of polarized interface in WS_2/CrOCl heterostructure.[34] Fig. 2c presents the current–voltage (I–V) characteristics of the WS_2/CrOCl interface under dark conditions and illumination with 680 nm laser. As shown in Fig. 2c, upon optical illumination, a typical short circuit current of 1 pA is clearly observed and the open-circuit voltage is 34 mV. The I–V curve is symmetric and linear without any rectification behaviour, indicating a negligible p–n junction effect in our devices.[50,51] The I–V curve also exhibits linearity over a wide range of drain-source voltages (see Fig. S4† for other scanning voltage ranges). In contrast to the I–V curve under optical illumination, the I–V curve shows minimal current over −200 mV to 200 mV, demonstrating that the observed current originates from photoexcitation.[25,52] The I–V curves under dark and illumination indicate the generation of BPVE in WS_2/CrOCl heterostructures. The inherent C_3 rotational symmetry of WS_2 engenders highly isotropic properties. Moreover, the C_3 symmetry cancels out the in-plane photovoltage, resulting in zero BPVE.[31] Photocurrent is not expected to generate for pristine WS_2 under laser illumination and zero bias. Similarly, MoS_2 and WSe_2, which possess same crystal symmetry as WS_2, have been demonstrated to exhibit no spontaneous photocurrent under zero bias.[30,31,35] Therefore,

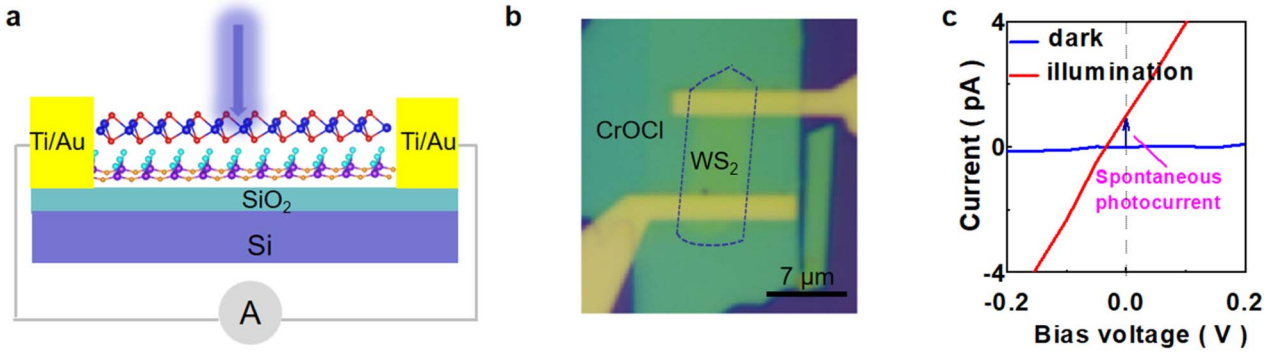

Fig. 2 BPVE generation in WS_2/CrOCl heterostructures. (a) Schematic diagram of the photocurrent measuring experiment. The circled "A" shows the electrical system for photocurrent measurement. (b) Optical microscope image of WS_2/CrOCl device. The yellow rectangle represents the electrodes, where the electrodes are parallel to the mirror plane of the device. (c) Current–voltage (I–V) curves of the WS_2/CrOCl device under dark conditions and laser irradiation with 60 mW cm^{-2}.

BPVE may be attributed to the in-plane polarization at the interface.[30]

3.3 Properties of photocurrent in WS_2/CrOCl devices

To reveal the mechanism of photocurrent, the spatial photocurrent response was measured by photocurrent mapping using a focused laser with the 532 nm. In our experiment, linearly polarized light was applied to the device (Fig. 3a). The noticeable photocurrent was observed across the entire channel between two electrodes without external bias, indicating in-plane charge carrier separation (Fig. 3b). This phenomenon excludes that the photocurrent originates from the p–n

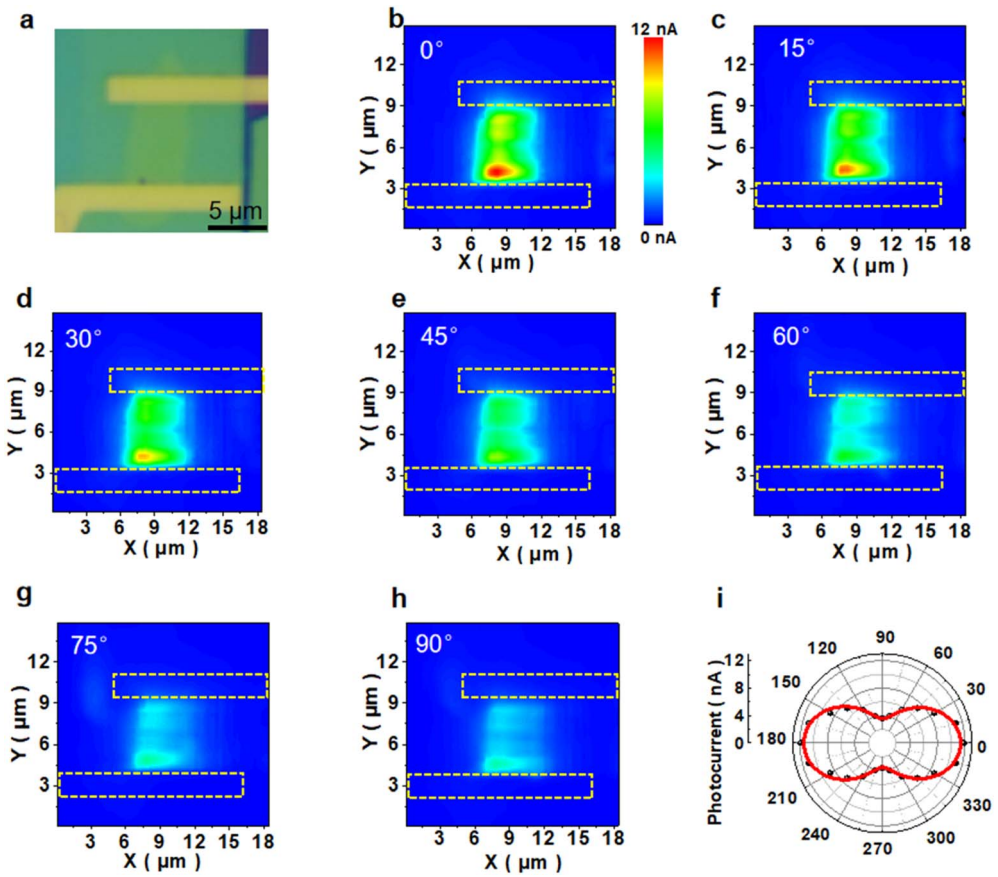

Fig. 3 Light angle dependence BPVE of WS_2/CrOCl device. (a) A schematic illustration of the photocurrent measuring experiment under polarized configuration. (b to h) Photocurrent mappings with the polarized angle ranging from 0° to 90° with the 532 nm laser. (i) Polar plot showing the photocurrent as a function of the linearly polarized angle (θ). The data are extracted from (b–h).

junction, consistent with the *I–V* curve[53] (Fig. 2c). The photocurrent line profile was extracted along the red line (Fig. S5†) where a weaker photocurrent was detected at the edge of the channel and the higher photocurrent intensity was away from the edge, similar to the current distribution in the ReS_2/ReS_2 edge-embedded structure.[54] These results indicate that Schottky barrier is not origin for the photocurrent generation.[55–58] The photocurrent distribution reflects a clear BPVE. Notably, as shown in Fig. 3b, the photocurrent generation is generally homogeneous across the channel, but, instead a pronounced local enhancement where photocurrent reaches 11.7 nA is visible. We attribute this enhancement to stronger interlayer in interaction between WS_2 flake and CrOCl flake as the laser dwell time in this region was slightly longer,[59] which likely led to tighter interfacial contact, enhancing the efficiency of photogenerated carrier transfer and extraction.

In order to understand the properties of BPVE, the spatial photocurrent response was measured at seven distinct angles. An initial incident light is primitively parallel to mirror plane of heterostructure and a half-wave plate is utilized to modulate the polarized angle θ of incident light. As the angle increases, the photocurrent response decreases noticeably from 11.7 nA to 3.5 nA at the same point of the entire channel in Fig. 3c–h. The photocurrent value of this heterostructure is on the same order of magnitude as those reported for WS_2/MoS_2 [31] and MoS_2/BP[35] heterostructure devices. Furthermore, the differential photocurrent to linearly polarized light of different polarization directions originates from symmetry breaking which endows the heterostructure with unique anisotropic physical properties. By extracting the photocurrent data from Fig. 3b–h and additional measurements with other angles at the same point, the photocurrent polar plot with representative twofold symmetry was constructed, which shows distinct polarized angle dependence (Fig. 3i). The angle-dependent photoresponse arises from symmetry breaking, which induces anisotropy in optical absorption, electronic band structure, and carrier transport.[60] Given the polarized strong angle dependence of the photocurrent, previous studies have proposed the shift current mechanism as the primary origin of BPVE.[4,61,62] Anisotropy ratio is defined as the ratio between the maximum and minimum value of the photocurrent (I_{max}/I_{min}). The anisotropy of WS_2/CrOCl heterostructure reaches around 3.29 which is comparable to the maximum anisotropy ratio of 3.74 reported for the SbI_3/Sb_2O_3 core–shell van der Waals heterojunction.[63,64] This result indicates that the WS_2/CrOCl heterostructure holds great potential for applications in polarization-sensitive photodetectors or bulk photovoltaic devices. Moreover, vdW materials possess a range of favorable properties. The synthesis of high-symmetry vdW materials (such as WS_2, MoS_2) has been relatively well-established, because their in-plane growth is largely isotropic which stems from the high-symmetry internal crystal structures.[65–68] In addition, because of the dangling-bond-free surface, the construction of vdW heterostructure is free from lattice-matching constraints.[60,69] Furthermore, stacking vdW materials with different rotational symmetries can reduce symmetry of the heterojunction interface. In this consideration, 2D vdW heterostructure provides multiple potential platforms for the exploration of polarized light sensing. Relevant studies demonstrate that channel thickness and device length critically influence photoelectric response of heterostructure. In-plane polarization remains confined to just a few atomic layers near the heterointerface.[35,70] Increasing thickness of the upper material allows lattice relaxation to progressively screen the interface-induced symmetry breaking in distal regions, reducing overall symmetry-breaking degree in heterostructures and weakening its photoelectric response.[70] While longer channels sustain higher open-circuit photovoltages, excessive length promotes carrier recombination, ultimately decreasing spontaneous current intensity.[71] These findings suggest that optimizing both channel thickness and device geometry could significantly improve the bulk photovoltaic effect, though systematic investigation remains necessary.

3.4 Polarization properties of heterostructure

To reveal the origin of BPVE in the WS_2/CrOCl nanoflakes, piezoresponse force microscopy (PFM) measurements were performed. PFM amplitude reflects the magnitude of the local piezoelectric response, while the phase indicates the polarization direction.[72,73] Fig. S6† shows an AFM image of the WS_2/CrOCl heterostructure with atomically smooth terraces. We measure step heights of 0.78 nm and 1.5 nm. Based on the step heigh, it was determined that the heterostructure is composed of WS_2 with varying thickness (two-layer WS_2 and three-layer WS_2) and CrOCl. In addition, thanks to its excellent mechanical flexibility and high in-plane stiffness, WS_2 can bend and conform naturally at the CrOCl/SiO_2 interface even when partially lying on the SiO_2 substrate, thereby avoiding structural fracture or significant strain.[74,75] Fig. 4d shows the out-of-plane (OOP) PFM amplitude and phase, measured by the vertical motions of the probe on the previously presented ultrathin sample. Overall, no significant phase contrast was observed in the OOP directions, confirming that there may be no out-of-plane polarization in the heterostructure. This result is consistent with WSe_2/BP heterostructure.[30] Fig. 4b and c display the in-plane (IP) PFM amplitude and phase by twisting the motion of probes. No response is induced when the polarization direction is perpendicular to the torsion axis and an induced response occurs when it is parallel (Fig S7†). The IP PFM phase image (Fig. 4b) is characterized by three color tones, reflecting that the phase contrast and reveal IP polarization in the sample. Moreover, the phase contrast shows thickness-dependent behavior. When the sample was rotated by 90°, PFM measurements were conducted again (Fig. 4c). No phase contrast was observed in the three regions as the torsion direction of the probe is perpendicular to the polarization direction. These results indicate that WS_2 exhibits in-plane polarization. The broken-symmetry at the interface leads to in-plane polarization, which gives rise to a built-in electric field.[30,32,35] Specifically, the built-in electric field can help separate photogenerated carriers from the interface and form the photocurrent. When polarized light is incident on the sample, the photogenerated carriers will move along the polarization direction (Fig. 4e). Therefore, the photocurrent will be generated along the in-plane polar direction at low-symmetry heterointerface.[30] The result also explains

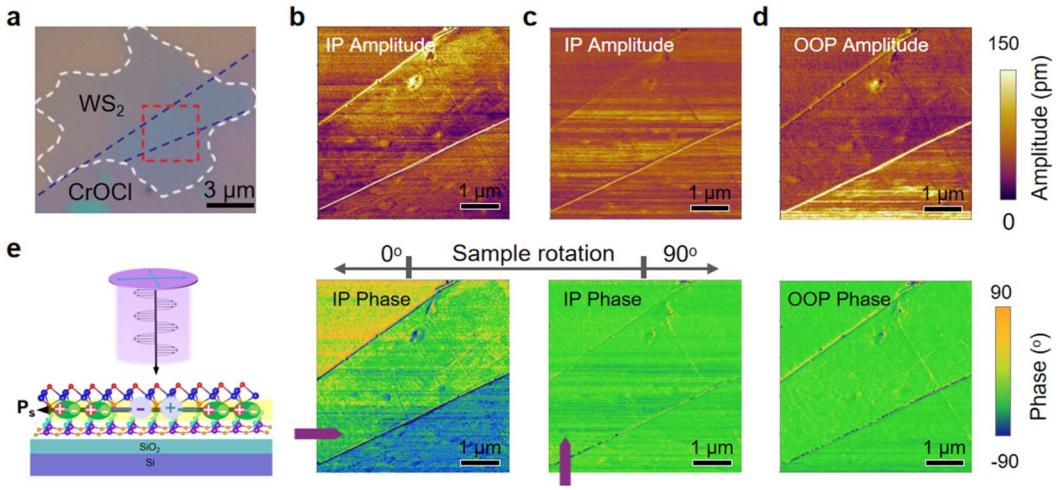

Fig. 4 PFM investigation of WS_2/CrOCl heterostructure. (a) An optical image of the WS_2/CrOCl materials. The region indicated by the red dashed box represents the PFM scanning area. (b) In-plane PFM with the amplitude image on top and the phase image below. (c) In-plane PFM after rotating the sample by 90° in (b) with the amplitude image on top and the phase image below. The purple arrow represents the direction of the probe movement in the (b and c). (d) Corresponding OOP PFM image with the amplitude image on top and the phase image below. Scale bars are 1 μm in (a–d). (e) Polarization schematic of the heterostructure. The green elliptical region represents the electric dipole moment. The red and green circular regions correspond to the bound positive charges and bound negative charges, while the purple '−' and emerald green '+' represent the negative photogenerated carriers and positive photogenerated carriers, respectively. The black arrow indicates the direction of in-plane polarization.

the significant variation of the photocurrent with changes in the polarized angle in Fig. 3.

4 Conclusions

In summary, we report a novel heterostructure system that successfully achieves BPVE and explore its underlying mechanism. Under zero bias, spontaneous photocurrent generation was successfully induced by breaking the WS_2/CrOCl interfacial symmetry, indicating the formation of BPVE in this heterostructure. As the angle increases, the photocurrent response decreases noticeably from 11.7 nA to 3.5 nA. Furthermore, the photocurrent distribution shows a significant angle dependence with anisotropy ratio of 3.29 at different incident angle. The BPVE is caused by in-plane polarization, which is induced by symmetry breaking engineering. Our research provides a new sight for a potential candidate for polarized light detection.

Data availability

The data that support the findings of this study are available from the corresponding author upon reasonable request.

Author contributions

Hong Zhou, Wei Luo: data curation, writing – original draft preparation. Xiaoming Zheng, Congbing Tan: validation, conceptualization, methodology, funding acquisition, project administration. Zhiyuan Dou, Zhongqiang Hu, Qianyi Li: supervision, software. Yuehua Wei: writing – reviewing and editing.

Conflicts of interest

The authors declare that they have no known competing financial interests or personal relationships that could have appeared to influence the work reported in this paper.

Acknowledgements

This work was supported by the National Natural Science Foundation of China (No. 62304198), Natural Science Foundation of Hunan Provincial (No. 2024JJ5164 and 2025JJ60432), Hunan Provincial Department of Education Excellent Young Scientist Fund (No. 22B0501), and the Changsha Natural Science Fund (No. kq2402081)

Notes and references

1 W. Shockley and H. Queisser, *Renewable Energy*, 2018, **32**, 35–54.
2 K. F. Mak and J. Shan, *Nat. Photonics*, 2016, **10**, 216–226.
3 H. Ai, Y. Kong, D. Liu, F. Li, J. Geng, S. Wang, K. H. Lo and H. Pan, *J. Phys. Chem. C*, 2020, **124**, 11221–11228.
4 G. Godefroy, *Ferroelectrics*, 1993, **141**, 345–347.
5 H. Li, C. R. Bowen and Y. Yang, *Adv. Funct. Mater.*, 2021, **31**, 2100905.
6 P. K. Nayak, S. Mahesh, H. J. Snaith and D. Cahen, *Nat. Rev. Mater.*, 2019, **4**, 269–285.
7 T. Choi, S. Lee, Y. Choi, V. Kiryukhin and S. Cheong, *Science*, 2009, **324**, 63–66.
8 M. Alexe and D. Hesse, *Nat. Commun.*, 2011, **2**, 256.

9 A. Zenkevich, Y. Matveyev, K. Maksimova, R. Gaynutdinov, A. Tolstikhina and V. Fridkin, *Phys. Rev. B:Condens. Matter Mater. Phys.*, 2014, **90**, 161409.
10 J. E. Spanier, V. M. Fridkin, A. M. Rappe, A. R. Akbashev, A. Polemi, Y. Qi, Z. Gu, S. M. Young, C. J. Hawley and D. Imbrenda, *Nat. Photonics*, 2016, **10**, 611–616.
11 P. Wurfel and I. Batra, *Ferroelectrics*, 1976, **12**, 55–61.
12 I. Grinberg, D. V. West, M. Torres, G. Gou, D. M. Stein, L. Wu, G. Chen, E. M. Gallo, A. R. Akbashev, P. K. Davies, J. E. Spanier and A. M. Rappe, *Nature*, 2013, **503**, 509–512.
13 Y. Bai, H. Jantunen and J. Juuti, *ChemSusChem*, 2019, **12**, 2540–2549.
14 H. Han, S. Song, J. H. Lee, K. J. Kim, G.-W. Kim, T. Park and H. M. Jang, *Chem. Mater.*, 2015, **27**, 7425–7432.
15 C. Li, Q. Cao, F. Wang, Y. Xiao, Y. Li, J. J. Delaunay and H. Zhu, *Chem. Soc. Rev.*, 2018, **47**, 4981–5037.
16 J. Zhang, S.-s. Li, W.-x. Ji, C.-w. Zhang, P. Li, S.-f. Zhang, P.-j. Wang and S.-s. Yan, *J. Mater. Chem. C*, 2017, **5**, 8847–8853.
17 F. Lyu, Y. Sun, Q. Yang, B. Tang, M. Li, Z. Li, M. Sun, P. Gao, L. Ye and Q. Chen, *Nanotechnology*, 2020, **31**, 315711.
18 S. N. Shirodkar and U. V. Waghmare, *Phys. Rev. Lett.*, 2014, **112**, 157601.
19 W. Ding, J. Zhu, Z. Wang, Y. Gao, D. Xiao, Y. Gu, Z. Zhang and W. Zhu, *Nat. Commun.*, 2017, **8**, 14956.
20 H. Wang, S. Wu, Y. Chen, Q. Zhao, J. Zeng, R. Yin, Y. Zheng, C. Liu, S. Zhang, T. Lin, H. Shen, X. Meng, J. Ge, X. Wang, J. Chu and J. Wang, *Sci. China Inf. Sci.*, 2025, **68**, 1–8.
21 N. Urakami, S. Ozaki and Y. Hashimoto, *Appl. Phys. Lett.*, 2024, **125**, 073102.
22 Z. Lei, Y. Xi, M. Shi, G. Xu, Y. Huang and X. Xu, *Adv. Mater.*, 2025, **37**, 2416595.
23 Z. Wang and Z. Liu, *J. Phys. Chem. Lett.*, 2023, **14**, 7549–7555.
24 J. Xu, Z. Yang, W. Liu, L. Wang and Y. Wang, *J. Phys.: Condens. Matter*, 2024, **36**, 205505.
25 C. Liu, T. Liang, X. Sui, L. Du, Q. Guo, G. Xue, C. Huang, Y. You, G. Yao, M. Zhao, J. Yin, Z. Sun, H. Hong, E. Wang and K. Liu, *Nat. Commun.*, 2025, **16**, 544.
26 H. Zhao, G. Zhang, B. Yan, B. Ning, C. Wang, Y. Zhao and X. Shi, *Research*, 2022, **2022**, 9840970.
27 J. Z. Zhao, L. C. Chen, B. Xu, B. B. Zheng, J. Fan and H. Xu, *Phys. Rev. B*, 2020, **101**, 121407.
28 J. Jiang, Z. Chen, Y. Hu, Y. Xiang, L. Zhang, Y. Wang, G. C. Wang and J. Shi, *Nat. Nanotechnol.*, 2021, **16**, 894–901.
29 R.-C. Xiao, Y. Gao, H. Jiang, W. Gan, C. Zhang and H. Li, *npj Comput. Mater.*, 2022, **8**, 138.
30 T. Akamatsu, T. Ideue, L. Zhou, Y. Dong, S. Kitamura, M. Yoshii, D. Yang, M. Onga, Y. Nakagawa, K. Watanabe, T. Taniguchi, J. Laurienzo, J. Huang, Z. Ye, T. Morimoto, H. Yuan and Y. Iwasa, *Science*, 2021, **372**, 68–72.
31 S. Zhang, M. Maruyama, S. Okada, M. Xue, K. Watanabe, T. Taniguchi, K. Hashimoto, Y. Miyata, R. Canton-Vitoria and R. Kitaura, *Nanoscale*, 2023, **15**, 5948–5953.
32 X. Huang, Q. Wang, K. Song, Q. Hu, H. Zhang, X. Gao, M. Long, J. Xu, Z. Chen, G. Zhou and B. Wu, *Nano Lett.*, 2025, **25**, 1495–1503.
33 S. Duan, F. Qin, P. Chen, X. Yang, C. Qiu, J. Huang, G. Liu, Z. Li, X. Bi, F. Meng, X. Xi, J. Yao, T. Ideue, B. Lian, Y. Iwasa and H. Yuan, *Nat. Nanotechnol.*, 2023, **18**, 867–874.
34 X. Zheng, Y. Wei, X. Zhang, Z. Wei, W. Luo, X. Guo, J. Liu, G. Peng, W. Cai, H. Huang, T. Lv, C. Deng and X. Zhang, *Adv. Funct. Mater.*, 2022, **32**, 2202658.
35 Z. Zeng, Z. Tian, Y. Wang, C. Ge, F. Strauß, K. Braun, P. Michel, L. Huang, G. Liu and D. Li, *Nat. Commun.*, 2024, **15**, 5355.
36 N. Miao, B. Xu, L. Zhu, J. Zhou and Z. Sun, *J. Am. Chem. Soc.*, 2018, **140**, 2417–2420.
37 T. Zhang, Y. Wang, H. Li, F. Zhong, J. Shi, M. Wu, Z. Sun, W. Shen, B. Wei, W. Hu, X. Liu, L. Huang, C. Hu, Z. Wang, C. Jiang, S. Yang, Q.-m. Zhang and Z. Qu, *ACS Nano*, 2019, **13**, 11353–11362.
38 X. Qing, H. Li, C. Zhong, P. Zhou, Z. Dong and J. Liu, *Phys. Chem. Chem. Phys.*, 2020, **22**, 17255–17262.
39 K. Yang, X. Gao, Y. Wang, T. Zhang, Y. Gao, X. Lu, S. Zhang, J. Liu, P. Gu and Z. Luo, *Nat. Commun.*, 2023, **14**, 2136.
40 Y. Cao, V. Fatemi, S. Fang, K. Watanabe, T. Taniguchi, E. Kaxiras and P. Jarillo-Herrero, *Nature*, 2018, **556**, 43–50.
41 Z. Qiu, M. Trushin, H. Fang, I. Verzhbitskiy, S. Gao, E. Laksono, M. Yang, P. Lyu, J. Li and J. Su, *Sci. Adv.*, 2019, **5**, eaaw2347.
42 Y. Liu, J. Rodrigues, Y. Z. Luo, L. Li, A. Carvalho, M. Yang, E. Laksono, J. Lu, Y. Bao and H. Xu, *Nat. Nanotechnol.*, 2018, **13**, 828–834.
43 W. Yu, S. Wang, Z. Liang, X. Cui, Y. Cui, F. Chen, C. Pan, S.-J. Liang and B. Cheng, *Appl. Phys. Lett.*, 2025, **126**, 053103.
44 Z. Zhang, A. Zobelli, C. Gao, Y. Cheng, J. Zhang, J. Caillaux, L. Qiu, S. Li, M. Cattelan, V. Kandyba, A. Barinov, M. Zaghrioui, A. Bendounan, J.-P. Rueff, W. Qi, L. Perfetti, E. Papalazarou, M. Marsi and Z. Chen, *Nat. Commun.*, 2025, **16**, 763.
45 R. Plumadore, M. M. Al Ezzi, S. Adam and A. Luican-Mayer, *J. Appl. Phys.*, 2020, **128**, 044303.
46 Y. Li, Y. Rao, K. F. Mak, Y. You, S. Wang, C. R. Dean and T. F. Heinz, *Nano Lett.*, 2013, **13**, 3329–3333.
47 X. Zhou, J. Cheng, Y. Zhou, T. Cao, H. Hong, Z. Liao, S. Wu, H. Peng, K. Liu and D. Yu, *J. Am. Chem. Soc.*, 2015, **137**, 7994–7997.
48 Y. Zhang, H. Li, L. Wang, H. Wang, X. Xie, S.-L. Zhang, R. Liu and Z.-J. Qiu, *Sci. Rep.*, 2015, **5**, 7938.
49 V. Shautsova, T. Sidiropoulos, X. Xiao, N. A. Güsken, N. C. G. Black, A. M. Gilbertson, V. Giannini, S. A. Maier, L. F. Cohen and R. F. Oulton, *Nat. Commun.*, 2018, **9**, 5190.
50 R. Frisenda, A. J. Molina-Mendoza, T. Mueller, A. Castellanos-Gomez and H. S. J. van der Zant, *Chem. Soc. Rev.*, 2018, **47**, 3339–3358.
51 A. J. Molina-Mendoza, E. Giovanelli, W. S. Paz, M. A. Niño, J. O. Island, C. Evangeli, L. Aballe, M. Foerster, H. S. J. van der Zant, G. Rubio-Bollinger, N. Agraït, J. J. Palacios, E. M. Pérez and A. Castellanos-Gomez, *Nat. Commun.*, 2017, **8**, 14409.
52 Y. Deng, Z. Luo, N. J. Conrad, H. Liu, Y. Gong, S. Najmaei, P. M. Ajayan, J. Lou, X. Xu and P. D. Ye, *ACS Nano*, 2014, **8**, 8292–8299.

53 M. Onoda and K. Tada, *Curr. Appl. Phys.*, 2003, **3**, 141–147.
54 Z. Liang, X. Zhou, L. Zhang, X. L. Yu, Y. Lv, X. Song, Y. Zhou, H. Wang, S. Wang, T. Wang, P. P. Shum, Q. He, Y. Liu, C. Zhu, L. Wang and X. Chen, *Nat. Commun.*, 2023, **14**, 4230.
55 Y. J. Zhang, T. Ideue, M. Onga, F. Qin, R. Suzuki, A. Zak, R. Tenne, J. H. Smet and Y. Iwasa, *Nature*, 2019, **570**, 349–353.
56 Q. Ma, S.-Y. Xu, C.-K. Chan, C.-L. Zhang, G. Chang, Y. Lin, W. Xie, T. Palacios, H. Lin, S. Jia, P. A. Lee, P. Jarillo-Herrero and N. Gedik, *Nat. Phys.*, 2017, **13**, 842–847.
57 H. Yuan, X. Wang, B. Lian, H. Zhang, X. Fang, B. Shen, G. Xu, Y. Xu, S. C. Zhang, H. Y. Hwang and Y. Cui, *Nat. Nanotechnol.*, 2014, **9**, 851–857.
58 E. Parzinger, M. Hetzl, U. Wurstbauer and A. W. Holleitner, *npj 2D Mater. Appl.*, 2017, **1**, 40.
59 Z. Wu, N. Zhu, J. Jiang, A. Zafar, J. Hong and Y. Zhang, *APL Mater.*, 2019, **7**, 041108.
60 Y. Ma, H. Yi, H. Liang, W. Wang, Z. Zheng, J. Yao and G. Yang, *Mater. Futures*, 2024, **3**, 012301.
61 P. Lopez-Varo, L. Bertoluzzi, J. Bisquert, M. Alexe, M. Coll, J. Huang, J. A. Jimenez-Tejada, T. Kirchartz, R. Nechache and F. Rosei, *Phys. Rep.*, 2016, **653**, 1–40.
62 L. Z. Tan, F. Zheng, S. M. Young, F. Wang, S. Liu and A. M. Rappe, *npj Comput. Mater.*, 2016, **2**, 1–12.
63 M. Xiao, H. Yang, W. Shen, C. Hu, K. Zhao, Q. Gao, L. Pan, L. Liu, C. Wang, G. Shen, H.-X. Deng, H. Wen and Z. Wei, *Small*, 2020, **16**, 1907172.
64 B. Cao, Q. Liu, Y. Zheng, X. Tang, J. Chai, S. Ma, W. Wang and G. Li, *Adv. Funct. Mater.*, 2022, **32**, 2110715.
65 T.-A. Chen, C.-P. Chuu, C.-C. Tseng, C.-K. Wen, H. S. P. Wong, S. Pan, R. Li, T.-A. Chao, W.-C. Chueh, Y. Zhang, Q. Fu, B. I. Yakobson, W.-H. Chang and L.-J. Li, *Nature*, 2020, **579**, 219–223.
66 T. Li, W. Guo, L. Ma, W. Li, Z. Yu, Z. Han, S. Gao, L. Liu, D. Fan, Z. Wang, Y. Yang, W. Lin, Z. Luo, X. Chen, N. Dai, X. Tu, D. Pan, Y. Yao, P. Wang, Y. Nie, J. Wang, Y. Shi and X. Wang, *Nat. Nanotechnol.*, 2021, **16**, 1201–1207.
67 J. Wang, X. Xu, T. Cheng, L. Gu, R. Qiao, Z. Liang, D. Ding, H. Hong, P. Zheng, Z. Zhang, Z. Zhang, S. Zhang, G. Cui, C. Chang, C. Huang, J. Qi, J. Liang, C. Liu, Y. Zuo, G. Xue, X. Fang, J. Tian, M. Wu, Y. Guo, Z. Yao, Q. Jiao, L. Liu, P. Gao, Q. Li, R. Yang, G. Zhang, Z. Tang, D. Yu, E. Wang, J. Lu, Y. Zhao, S. Wu, F. Ding and K. Liu, *Nat. Nanotechnol.*, 2022, **17**, 33–38.
68 J. Li, M. Chen, A. Samad, H. Dong, A. Ray, J. Zhang, X. Jiang, U. Schwingenschlögl, J. Domke, C. Chen, Y. Han, T. Fritz, R. S. Ruoff, B. Tian and X. Zhang, *Nat. Mater.*, 2022, **21**, 740–747.
69 W. Xin, W. Zhong, Y. Shi, Y. Shi, J. Jing, T. Xu, J. Guo, W. Liu, Y. Li, Z. Liang, X. Xin, J. Cheng, W. Hu, H. Xu and Y. Liu, *Adv. Mater.*, 2024, **36**, 2306772.
70 Z. Li, J. Huang, L. Zhou, Z. Xu, F. Qin, P. Chen, X. Sun, G. Liu, C. Sui, C. Qiu, Y. Lu, H. Gou, X. Xi, T. Ideue, P. Tang, Y. Iwasa and H. Yuan, *Nat. Commun.*, 2023, **14**, 5568.
71 A. Pusch, U. Römer, D. Culcer and N. J. Ekins-Daukes, *PRX Energy*, 2023, **2**, 013006.
72 A. Gruverman and S. V. Kalinin, *J. Mater. Sci.*, 2006, **41**, 107–116.
73 D. Denning, J. Guyonnet and B. J. Rodriguez, *Int. Mater. Rev.*, 2024, **61**, 46–70.
74 A. Falin, M. Holwill, H. Lv, W. Gan, J. Cheng, R. Zhang, D. Qian, M. R. Barnett, E. J. G. Santos, K. S. Novoselov, T. Tao, X. Wu and L. H. Li, *ACS Nano*, 2021, **15**, 2600–2610.
75 R. Oliva, T. Wozniak, P. E. Faria Jr, F. Dybala, J. Kopaczek, J. Fabian, P. Scharoch and R. Kudrawiec, *ACS Appl. Mater. Interfaces*, 2022, **14**, 19857–19868.